Strain tunability of magnetocrystalline anisotropy in Fe_3GeTe_2 thin films

Bomin Kim,[1] Qurat ul ain,[1,2] and S. H. Rhim[1,*]
[1]*Department of Physics, University of Ulsan, Ulsan 44610, Republic of Korea*
[2]*Department of Physics, Quaid-i-Azam University, Islamabad 45320, Pakistan*

(Received 9 January 2024; accepted 29 April 2024; published 20 May 2024)

Strain tunability of magnetocrystalline anisotropy (MCA) in Fe_3GeTe_2 is demonstrated for monolayer and bilayer structures. In the framework of density functional calculations, upon in-plane strain η, $-5\% \leqslant \eta \leqslant +5\%$, MCA exhibits contrasting behaviors for compressive and tensile strains. For tensile strain ($\eta > 0$), perpendicular MCA is well retained with little change in the magnetic moments. For compressive strain ($\eta < 0$), on the other hand, an abrupt decrease in E_{MCA} and change in the magnetic moments are prominent. It is noteworthy that bilayer Fe_3GeTe_2 even exhibits a sign change of E_{MCA}, indicating a transformation from perpendicular to in-plane magnetization. The feature of MCA is analyzed from three perspectives: (1) atomic decomposition, (2) the spin-orbit coupling (SOC) matrix in the d and p manifolds, and (3) occupation changes in the band structure. In atomic decomposition, the Te contribution predominates and accompanies a sign change in the bilayer structure. The SOC matrix in Te p manifolds under the compressive strain $\langle m = \pm 1, \uparrow | L_z | m = \pm 1, \uparrow \rangle$ contribution to $E_{\mathrm{MCA}} > 0$ decreases. In the bilayer structure, $\langle m = \pm 1, \downarrow | L_x | m = 0, \downarrow \rangle$ is responsible for the sign change of E_{MCA} when $\eta = -5\%$.

DOI: 10.1103/PhysRevB.109.174434

I. INTRODUCTION

The discovery of magnetism in the two-dimensional (2D) material CrI_3 [1] has upset the common wisdom based on the Mermin-Wagner theorem that long-range order in a 2D system is impossible [2]. Other families of 2D magnets have been added, such as MPS_3 (M = Fe, Ni, Mn) [3–6], $CrGeTe_3$ [7], and so forth. Furthermore, these 2D magnets have offered a playground for long-standing many-body problems: the Ising model, XY model, and Heisenberg model as a test bed for the Onsager solution; the Berezinskii-Kosterlitz-Thouless transition [8]; and magnetic anisotropy [9–11].

Among 2D magnets, the new class Fe_3GeTe_2 (FGT) has attracted intense attention due to its relatively high T_C. Monolayer, bilayer, and bulk FGT have T_C of 130, 180, and 220 K, respectively [12–14]. Subsequent studies followed with interesting features: voltage-controlled magnetism [15], anomalous Hall conductivity with layer and thickness dependence [16], exchange bias [17], topological properties with nodal lines [18], and even possible noncollinear phases [19]. While several magnetic phases have been reported, magnetocrystalline anisotropy (MCA), which is promising for spintronics applications, has been explored theoretically and experimentally. Perpendicular MCA (PMCA) has been confirmed experimentally for bulk FGT [13,20] and theoretically for monolayer FGT [21,22].

In this paper, MCA of FGT is investigated using first-principles calculations. More specifically, the strain η tunability of MCA is explored for strains $-5\% \leqslant \eta \leqslant +5\%$. The electronic structure with respect to strain is fully examined. Strain-dependent magnetic moments are discussed. Then, an analysis of MCA is provided from three perspectives: (1) atomic decomposition, (2) the spin-orbit coupling (SOC) matrix in d-p manifolds, and (3) occupation changes in the band structure. In this way, the distinctive behavior of MCA energy E_{MCA} upon compressive and tensile strains is exhaustively investigated. We note that Te contributions play dominant roles as analyzed in Te p manifolds. Under compressive strain, $\langle m = \pm 1 | L_z | m = \pm 1 \rangle$ and $\langle m = 0 | L_x | m = \pm 1 \rangle$ to $E_{\mathrm{MCA}} > 0$ decrease. In the bilayer, $\langle m = 0 | L_x | m = \pm 1 \rangle$ is responsible for the sign change of E_{MCA} when $\eta = -5\%$.

II. CALCULATION METHOD AND STRUCTURE

Density functional calculations are carried out employing Vienna Ab initio Simulation Package (VASP) [23]. The local density approximation is used for the exchange-correlation potential. For the bilayer and bulk, the interlayer van der Waals interactions are treated using the van der Waals density functional (vdW-DF) based on the B86b exchange [24], vdW-DF-optB86 [25]. For the monolayer and bilayer, the vertical length is fixed at 30 Å, with vacuum spacing being more than 15 Å. For all cases, atomic positions are optimized with a force criterion of 5 meV/Å. The energy cutoff for plane wave expansion is 450 eV, and a $21 \times 21 \times 1$ k mesh in the Monkhorst-Pack scheme is used for Brillouin zone summation. For MCA [26,27] calculations, $E_{\mathrm{MCA}} = E(\rightarrow) - E(\uparrow)$ with SOC included, where $\rightarrow$ and $\uparrow$ stand for the direction of magnetization. The analysis of E_{MCA} is given in Sec. IV.

Bulk FGT crystallizes in a hexagonal structure with space group $P6_3/mmc$ (No. 194), as depicted in Fig. 1(a). Optimized lattice constants are $a = 4.00$ Å, $c = 16.31$ Å, and $c/a = 4.08$, which agree well with previous studies [13,21,28,29].

*sonny@ulsan.ac.kr

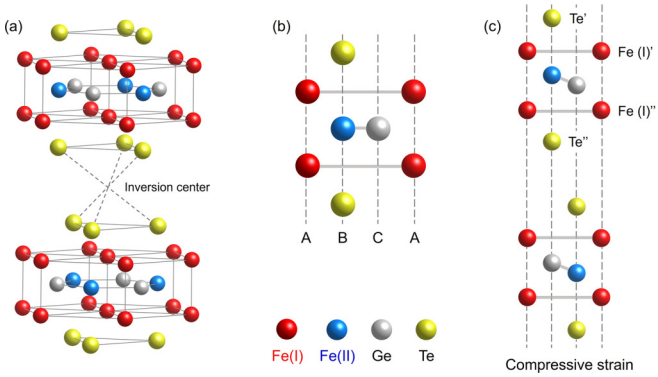

FIG. 1. (a) Crystal structure of bulk Fe_3GeTe_2 (FGT); bilayer and two monolayer units are connected by the inversion center. (b) Side view of one monolayer unit, where A, B, and C denote hexagonal sites. (c) Side view of the bilayer for compressive strain. Fe(I) and Te are further distinguished as inner and outer atoms by single and double primes.

Upon applying strain, compressive (tensile) strain along the in-plane direction results in expansion (contraction) of c/a as a result of the Poisson effect. The bulk structure consists of one bilayer or two monolayer units, which are connected by the inversion symmetry. The monolayer unit, with quintuple sublayers, is depicted in Fig. 1(b), where A, B, and C denote the hexagonal sites. Two symmetrically inequivalent Fe atoms are distinguished by Fe(I) and Fe(II). All atoms take hexagonal sites: Fe(I) for A, Fe(II) and Te for B, and Ge for C sites. The quintuple sublayers, one monolayer unit, have Fe(II)-Ge at the center, sandwiched by Fe(I) and Te above and below. Figure 1(c) presents the bilayer structure under compressive strain, where Fe(II)-Ge buckling manifests. The buckling further distinguishes Fe(I) and Te. We denote outer and inner atoms with respect to the inversion center by single and double primes, respectively. More specifically, atoms closer to Fe(II) are Fe(I)′ and Te′; those farther from Fe(II) are Fe(II)″ and Te″. This distinction is used for later discussion in Sec. III.

III. MAGNETISM AND ELECTRONIC STRUCTURE

In this section, we discuss the strain-dependent electronic structure and MCA of mono- and bilayer FGT. Table I lists the magnetic moments of the constituent atoms without strain for the monolayer, bilayer, and bulk. In all cases, Fe(I) has larger moments than Fe(II) by $1\mu_B$. Ge and Te have signs opposite those of Fe(I) and Fe(II) with magnitudes less than $0.1\mu_B$. The different magnitudes of Fe(I) and Fe(II) are due to

TABLE I. Magnetic moments (in units of μ_B) for monolayer, bilayer, and bulk FGT without strain. Fe(I) has a greater moment than Fe(II) in all structure types.

Structure	Monolayer	Bilayer	Bulk
Fe(I)	2.06	2.32	2.30
Fe(II)	1.04	1.34	1.37
Ge	−0.06	−0.09	−0.10
Te	−0.03	−0.04	−0.04

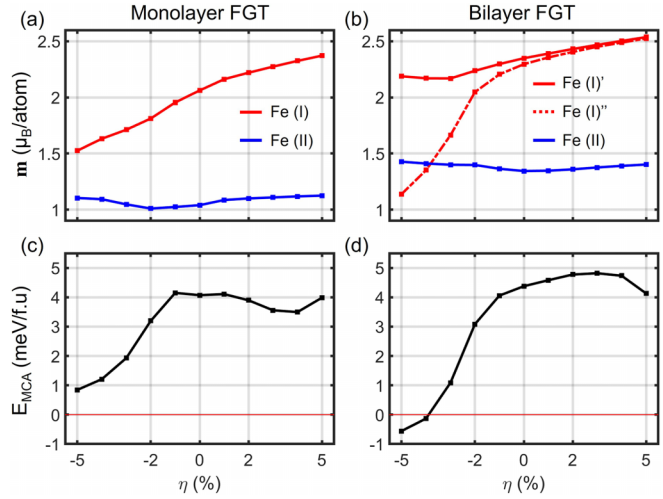

FIG. 2. Strain-dependent magnetism of FGT. Left and right panels show monolayer and bilayer FGT, respectively. (a) and (b) Magnetic moments and (c) and (d) magnetocrystalline anisotropy energy.

inequivalent site symmetry associated with neighboring atoms, which is briefly discussed in the Supplemental Material [30].

Figure 2 presents magnetic moments of Fe atoms and MCA for the monolayer and bilayer under strains ($-5\% \leqslant \eta \leqslant +5\%$). The left (right) panels show the monolayer (bilayer), and the top (bottom) panels show the magnetic moments (MCA). The total magnetic moment of the monolayer changes from $4.07\mu_B$ to $5.73\mu_B$/f.u.; that of the bilayer ranges from $4.56\mu_B$ to $6.26\mu_B$/f.u. Moments of Fe(I) and Fe(II) are distinguished by red and blue lines, respectively. In the bilayer, Fe(I)′ and Fe(I)″ are further distinguished by red solid and dashed lines, respectively. As in the case without strain listed in Table I, Fe(I) has a larger magnetic moment than Fe(II). Evidently, Fe(I) moments in the monolayer noticeably change from $1.53\mu_B$ to $2.37\mu_B$, where magnitude decreases (increases) under compressive (tensile) strain. In the bilayer, similar to the monolayer, Fe(II) moment remains relatively insensitive to strain, while the change in the Fe(I) moment is noticeable. However, the change in Fe(I)′ is smaller than that observed in the monolayer by $0.5\mu_B$. On the other hand, the change in the Fe(I)″ moment is drastic under compressive strain, ranging $1.14\mu_B$ to $2.53\mu_B$, which becomes smaller than Fe(II) when $\eta < -3\%$.

E_{MCA} with respect to strain is presented in Figs. 2(c) and 2(d). At $\eta = 0\%$, E_{MCA} of monolayer FGT is 4.07 meV/f.u., which agrees well with previous studies [21,22]. With strain, for the monolayer $0.85 \leqslant E_{\mathrm{MCA}} \leqslant 4.15$ meV/f.u., and for the bilayer $-0.56 \leqslant E_{\mathrm{MCA}} \leqslant 4.82$ meV/f.u. For tensile strain, $E_{\mathrm{MCA}} \approx 4$ meV/f.u., where the bilayer is slightly enhanced compared with the monolayer. For compressive strain, on the other hand, the decrease in E_{MCA} evident. E_{MCA} drops rapidly for both the monolayer and bilayer. For the monolayer, E_{MCA} drops to 0.85 meV/f.u., which is consistent with a previous study on monolayer FGT under compressive strain [21]. The decrease in the bilayer is so drastic that E_{MCA} has a sign change when $\eta < -3\%$. In addition, the angular dependence of MCA, $E_{\mathrm{MCA}}(\theta, \varphi) = E(\theta, \varphi) - E(\theta = 0,$

TABLE II. MCA coefficients K_1 and K_2 (in meV/f.u.) for FGT in the hexagonal system, $E_{\rm MCA}(\theta,\varphi) = K_1 \sin^2\theta + K_2 \sin^4\theta$, for strains of -5%, 0%, and $+5\%$.

	Monolayer FGT			Bilayer FGT		
	-5%	0%	$+5\%$	-5%	0%	$+5\%$
K_1	0.61	3.88	4.62	−0.19	3.92	4.42
K_2	0.07	0.19	−0.68	−0.08	−0.53	0.29

$\varphi = 0$), is investigated, where θ and φ are the polar and azimuthal angles of the magnetization axis. For a hexagonal system, $E_{\rm MCA}(\theta,\varphi) = K_1 \sin^2\theta + K_2 \sin^4\theta$ [31], where K_1 and K_2 are listed in Table II. For both mono- and bilayer FGT, the φ dependence of $E_{\rm MCA}$ is negligible, while the θ dependence exhibits significant change. Further details are given in the Supplemental Material [30]. MCA in Fig. 2 is further investigated in terms of the electronic structure analysis in Sec. IV.

The density of states (DOS) is analyzed in Figs. 3 and 4 for the monolayer and bilayer, respectively. Left panels show Fe(I) or Fe(I)″; right panels show Te or Te″. Three strains are presented: from top to bottom, $\eta = +5\%$, 0%, and -5%.

In hexagonal symmetry, the d orbital manifold has three representations according to the magnetic quantum number m: $m = 0$, ±1, and ±2, or d_{z^2}, $d_{xz/yz}$, and $d_{x^2-y^2/xy}$; the p manifold is represented by $m = 0$, and ±1, or p_z and $p_{x/y}$. In DOS plots, d and p orbitals are shown by solid and dashed lines, respectively, and important peaks are labeled by A, B, C, and their variants.

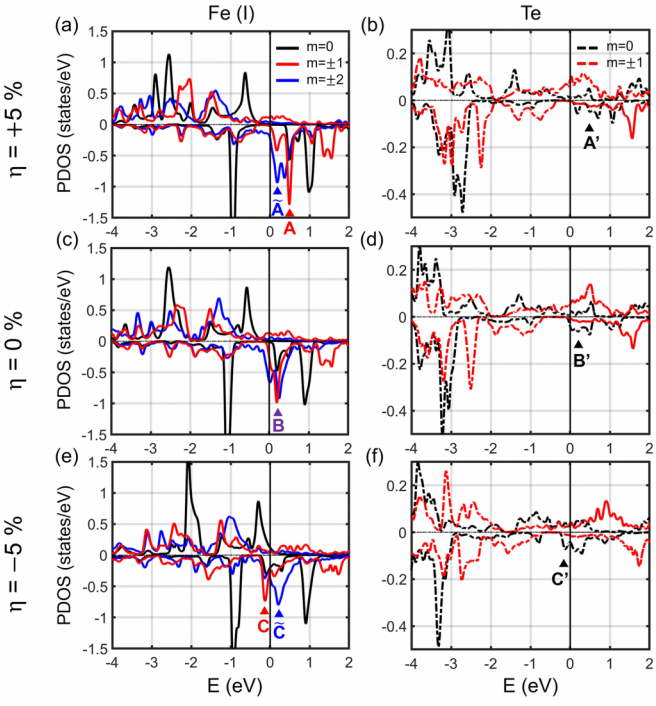

FIG. 3. Partial density of states (PDOS) of monolayer Fe_3GeTe_2. Left and right panels show Fe(I) and Te, respectively. (a) and (b) $\eta = +5\%$, (c) and (d) $\eta = 0\%$, and (e) and (f) $\eta = -5\%$. Solid and dashed lines denote d and p orbitals, respectively. Black, red, and blue lines denote $m = 0$, ±1, and ±2, respectively.

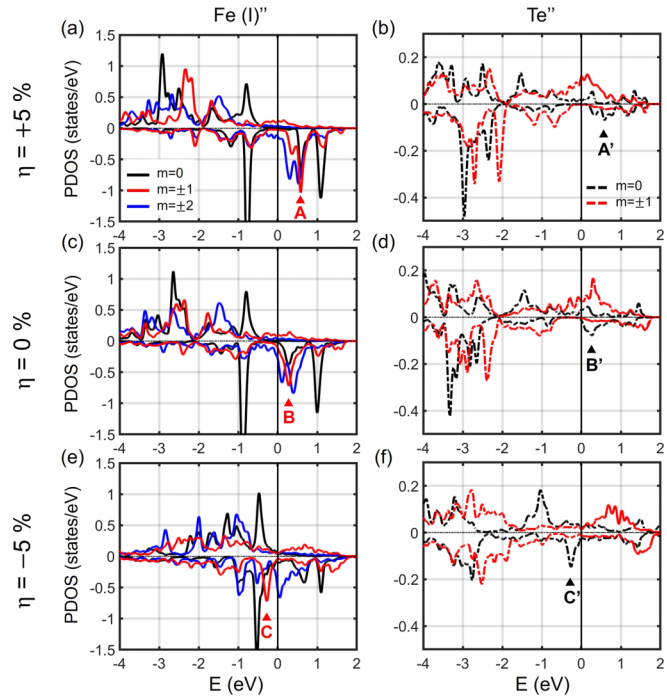

FIG. 4. PDOS of bilayer Fe_3GeTe_2. Left and right panels show Fe(I)″ and Te″, respectively. (a) and (b) $\eta = +5\%$, (c) and (d) $\eta = 0\%$, and (e) and (f) $\eta = -5\%$. Solid and dashed lines indicate d and p orbitals, respectively. Black, red, and blue lines denote $m = 0$, ±1, and ±2, respectively.

The partial DOS (PDOS) of monolayer FGT is plotted in Figs. 3(c) and 3(d) for $\eta = 0\%$, where important peaks in the minority spin state are marked as B and B' for Fe(I) d states ($d_{xz/yz}$ and $d_{x^2-y^2/xy}$) and Te p_z, respectively. Partially occupied peaks, B and B', are just above the Fermi energy E_F. For tensile strain, $\eta = +5\%$, the nearly degenerate B splits into A ($d_{xz/yz}$) and $\tilde{A}$ ($d_{x^2-y^2/xy}$), where A shifts by $+0.29$ eV with respect to B. Te B' also shifts by $+0.29$ eV, indicating Fe(I)-Te hybridization. For compressive strain, $\eta = -5\%$, the shifts of the peaks are opposite those for $\eta = +5\%$. C is occupied, whereas $\tilde{C}$ is still empty. Te p_z is more occupied with a left shift relative to $\eta = 0\%$ with partial occupation. Fe(I) C and Te C' shift by -0.31 eV with respect to B and B', respectively. This change in occupation of Fe(I) and Te accounts for the increase (decrease) of magnetic moment under tensile (compressive) strain. The occupation of the majority spin state changes little, but the decrease (increase) in the occupation of the minority spin state increases (reduces) the overall magnetic moments.

The PDOSs of bilayer FGT are shown in Fig. 4 for Fe(I)″ and Te″. As Fe(I)′ shows little change with strain, PDOSs of Fe(I)″ and Te″ are shown. For $\eta = 0\%$, B and B' are the peaks for Fe(I)″ $d_{xz/yz}$ and Te″ p_z in the minority spin state, respectively. Compared to Fe(I) and Te in the monolayer, the peaks of Fe(I)″ and Te″ are slightly shifted. For $\eta = 0\%$, B and B' are around $E_F + 0.29$ eV. The right shift is present for $\eta = +5\%$; A and A' are around $E_F + 0.59$ eV. For $\eta = -5\%$, however, a leftward shift becomes apparent; C and C' are at

$E_F - 0.28$ eV. The peak shifts discussed here are revisited later in Sec. IV. The peak shifts with Fe(I)-Te hybridization result in moment change. Peak changes with respect to occupation changes are qualitatively discussed in terms of the bond length or Fe(I)-Te distance.

Compressive (tensile) in-plane strain accompanies expansion (contraction) of the vertical length c as consequence of the Poisson effect. Distances between atoms change accordingly. In the monolayer, the Fe(I)-Te distance decreases (increases) under compressive (tensile) strain, ranging from 2.55 to 2.73 Å. In the bilayer, the Fe(I)′-Te′ and Fe(I)″-Te″ distances decrease (increase) under compressive (tensile) strain. Especially, compared to the Fe(I)′-Te′ distance, the Fe(I)″-Te″ distance shows a more drastic change from 2.60 to 2.76 Å. As shown by the PDOS (Figs. 3 and 4), hybridized peaks of Fe(I)-Te or Fe(I)″-Te″ shift rightward (leftward) as the distance between two atoms increases (decreases). Magnetic moments of Fe(I) and Fe(I)″ tend to increase (or decrease) with the distances of Fe(I)-Te and Fe(I)″-Te″, respectively, as shown in the Supplemental Material [30].

IV. MAGNETOCRYSTALLINE ANISOTROPY

MCA is calculated from the difference in total energies between in-plane ($\parallel$) and perpendicular ($\perp$) magnetization with SOC included,

$$E_{\mathrm{MCA}} = E(\parallel) - E(\perp). \tag{1}$$

Positive (negative) E_{MCA} implies perpendicular (in-plane) MCA. E_{MCA} is analyzed in the framework of the second-order perturbation theory [32],

$$E_{\mathrm{MCA}} = \xi^2 \sum_{\sigma,\sigma',o,u} \frac{|\langle o,\sigma|L_z|u,\sigma'\rangle|^2 - |\langle o,\sigma|L_x|u,\sigma'\rangle|^2}{E_{u,\sigma} - E_{o,\sigma'}}, \tag{2}$$

where ξ is the strength of SOC, o (u) stands for the occupied (unoccupied) state, σ and σ' denote spin states, L_z (L_x) is the orbital angular momentum operator for the z (x) component, and $E_{o,\sigma}$ ($E_{u,\sigma}$) is the energy of the occupied (unoccupied) state. Each $|o\rangle$ and $|u\rangle$ is expanded by $|l,m\rangle$ eigenstates,

$$|o\rangle = \sum_{l,m} o_{l,m}|l,m\rangle, \quad |u\rangle = \sum_{l',m'} u_{l',m'}|l',m'\rangle, \tag{3}$$

with $E_o < E_F$ and $E_u > E_F$. The matrices above are easily evaluated using eigenvalue equations for angular momentum in quantum mechanics [33]. L_z (L_x) is responsible for positive (negative) E_{MCA} with the same spin channel ($\sigma = \sigma'$), but L_z (L_x) is responsible for negative (positive) E_{MCA} with the spin-flip channel ($\sigma \neq \sigma'$).

Strain-dependent E_{MCA}, shown in Figs. 2(c) and 2(d), is analyzed in detail from three perspectives: (1) atomic decomposition, (2) the SOC matrix of the d and p manifolds, and (3) occupation changes in the band structure. Because the change in E_{MCA} is more pronounced under compressive strain, we compare $\eta = 0\%$ and $\eta = -5\%$. Atomic decomposition of E_{MCA} is presented in Fig. 5 for mono- and bilayer FGT. The atomic contribution is estimated from $E_{\mathrm{MCA}} \approx \frac{1}{2}\Delta E_{\mathrm{SOC}}$ [34], where $\Delta E^{\alpha}_{\mathrm{SOC}}$ is the difference in SOC energies of the atomic site α between in-plane and perpendicular magnetizations. For the monolayer, as seen in Fig. 5(a), the Fe(II) contribution

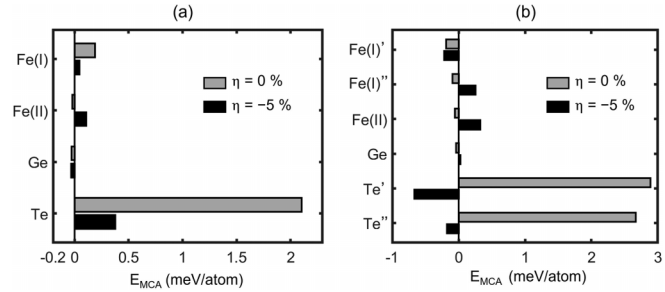

FIG. 5. Atom-decomposed E_{MCA} of Fe_3GeTe_2 for (a) the monolayer and (b) bilayer. Gray and black bars denote $\eta = 0\%$ and -5%, respectively. In both cases, at $\eta = -5\%$, the reduction of E_{MCA} is predominated by Te.

for $\eta = -5\%$ increases, while those of Fe(I) and Te decrease with respect to $\eta = 0\%$. It is noteworthy that the drop in E_{MCA} under compressive strain predominates from Te: from 2.11 to 0.38 meV/atom. Figure 5(b) shows atom decomposition for bilayer. The Fe(I)′ contribution does not change with strain. However, the Fe(I)″ and Fe(II) contributions for $\eta = -5\%$ increase, with a sign change from negative to positive. On the other hand, the decrease in the Te′ and Te″ contributions is significant, from 2.86 to -0.66 and 2.67 to -0.17 meV/atom, respectively.

Figure 6 shows orbital-projected SOC matrices in the Fe d and Te p manifolds, where the left (right) column shows $\eta = 0\%$ ($\eta = -5\%$). The upper (lower) box is for monolayer (bilayer) FGT. For the monolayer, when $\eta = 0\%$ [Fig. 6(a)], the Fe(I) contribution to $E_{\mathrm{MCA}} > 0$ comes mainly from $\langle m = \pm 2|L_z|m = \pm 2\rangle$, with some contribution from $\langle m =$

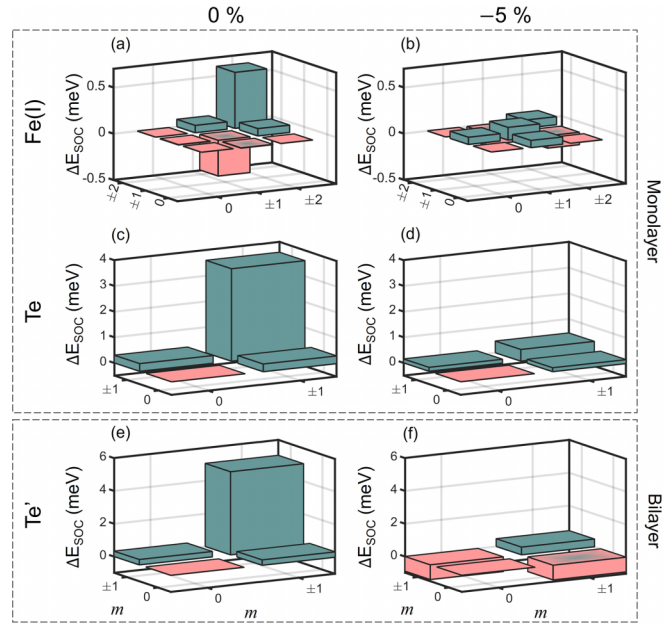

FIG. 6. Orbital-projected SOC matrices. Left and right panels show $\eta = 0\%$ and $\eta = -5\%$, respectively. Projection is done into the d manifold for Fe ($m = 0, \pm 1, \pm 2$) and the p manifold for Te ($m = 0, \pm 1$), following the irreducible representation of hexagonal symmetry. The upper (lower) box is for monolayer (bilayer) Fe_3GeTe_2. Green and red denote positive and negative E_{MCA}, respectively.

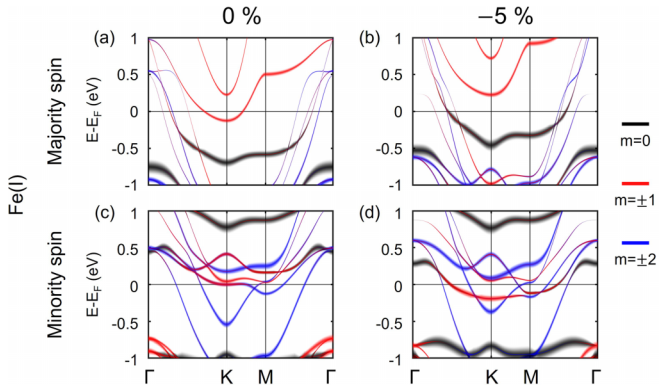

FIG. 7. The orbital-projected band structures (d orbital) for Fe(I) in the monolayer. The $m = 0, \pm 1$, and ± 2 orbital states are shown by black, red, and blue lines, respectively. Left and right panels show $\eta = 0\%$ and -5%, respectively. (a) and (b) The majority spin channel and (c) and (d) the minority spin channel.

$\pm 2|L_x|m = \pm 1\rangle$, whereas that to $E_{\rm MCA} < 0$ is mostly from $\langle m = \pm 1|L_z|m = \pm 1\rangle$. Under compressive strain [Fig. 6(b)], while a small $E_{\rm MCA} > 0$ comes from $\langle m = \pm 1|L_z|m = \pm 1\rangle$ and $\langle m = \pm 1|L_x|m = 0\rangle$, $E_{\rm MCA} > 0$ from $\langle m = \pm 2|L_z|m = \pm 2\rangle$ is notably reduced, along with $E_{\rm MCA} < 0$ from $\langle m = \pm 2|L_x|m = \pm 1\rangle$. Overall, $E_{\rm MCA} > 0$ from Fe(I) decreases under compressive strain. The Te contribution, on the other hand, is straightforward. There is no sign change, but the $\langle m = \pm 1|L_z|m = \pm 1\rangle$ contribution to $E_{\rm MCA} > 0$ decreases. Summing up, for the monolayer the decrease in $E_{\rm MCA}$ with compressive strain is mainly due to reduced $E_{\rm MCA} > 0$ contributions. For the bilayer, $E_{\rm MCA}$ contributions other than those for Te atoms do not decrease much when $\eta = -5\%$. As in the monolayer, Te′ $E_{\rm MCA}$ for $\eta = 0\%$ is predominated by $\langle m = \pm 1|L_z|m = \pm 1\rangle$. Under compressive strain, $\langle m = \pm 1|L_z|m = \pm 1\rangle$ decreases tremendously, and $E_{\rm MCA} < 0$ emerges from $\langle m = \pm 1|L_x|m = 0\rangle$. Thus, the sign change of $E_{\rm MCA}$ in the bilayer is mainly due to the emergence of $E_{\rm MCA} < 0$ from $\langle m = \pm 1|L_x|m = 0\rangle$.

We continue our MCA analysis based on band structure with k and orbital resolution. Figures 7 and 8 respectively show the Fe and Te contributions with projection of orbital characters. Figure 7 focuses on Fe(I) of the monolayer, where the d orbital is decomposed into magnetic quantum numbers $m = 0, \pm 1, \pm 2$ according to the irreducible representation. Top and bottom panels show the majority and minority spin channels, respectively. Hereafter, the majority and minority spin channels are denoted as ↑ and ↓, respectively.

When $\eta = 0\%$ [Figs. 7(a) and 7(c)], $m = \pm 1$ bands in the ↑ state for both occupied and unoccupied states give $E_{\rm MCA} > 0$ via $\langle m = \pm 1, \uparrow |L_z|m = \pm 1, \uparrow\rangle$. However, $m = \pm 1$ bands in the ↓ state for only the unoccupied state give $E_{\rm MCA} < 0$ via the spin-flip channel, $\langle m = \pm 1, \uparrow |L_z|m = \pm 1, \downarrow\rangle$. $m = \pm 2$ bands are predominant in the ↓ state, whose coupling $\langle m = \pm 2, \downarrow |L_z|m = \pm 2, \downarrow\rangle$ gives $E_{\rm MCA} > 0$. As shown in Fig. 6(a), $\langle m = \pm 2|L_z|m = \pm 2\rangle$ gives $E_{\rm MCA} > 0$ with the same spin channel, while $\langle m = \pm 1|L_z|m = \pm 1\rangle$ results in $E_{\rm MCA} < 0$ with the spin-flip channel.

When $\eta = -5\%$ [Figs. 7(b) and 7(d)], some bands change occupations. The $m = \pm 1$ band in the ↑ channel becomes unoccupied, and the $m = \pm 1$ band in the ↓ channel becomes occupied around K. Due to the occupation change, $\langle m = \pm 1, \downarrow |L_z|m = \pm 1, \downarrow\rangle$ contributes to $E_{\rm MCA} > 0$. Additionally, $E_{\rm MCA} < 0$ from $\langle m = \pm 1, \uparrow |L_z|m = \pm 1, \downarrow\rangle$ decreases. Occupied $m = \pm 2$ bands in the ↑ channel come near E_F due to an upward shift. $E_{\rm MCA} < 0$ comes from spin-flip channels, $\langle m = \pm 2, \uparrow |L_z|m = \pm 2, \downarrow\rangle$. As shown in Fig. 6(b), when $\eta = -5\%$, $E_{\rm MCA}$ from $m = \pm 1$ coupling become positive due to increased (decreased) contributions from the same spin (spin-flip) channels. On the other hand, $E_{\rm MCA}$ from $m = \pm 2$ coupling reduces due to negative contributions from the spin-flip channels.

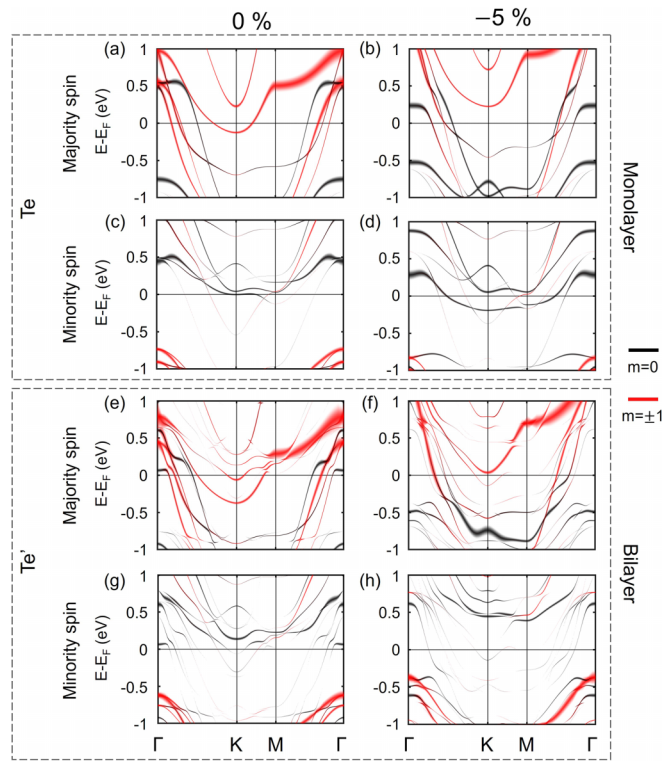

FIG. 8. The orbital-projected band structures (p orbital) for Te. The $m = 0$ and ± 1 orbital states are shown by black and red lines, respectively. Left and right panels show $\eta = 0\%$ and -5%, respectively. (a)–(d) Te in the monolayer and (e)–(h) Te′ in the bilayer, respectively.

Figure 8 shows Te contributions with p orbital projections in terms of magnetic quantum numbers $m = 0, \pm 1$. Figures 8(a)–8(d) [Figs. 8(e)–8(h)] show Te (Te′) in the monolayer (bilayer). In each box, the top (bottom) panels denote the ↑ (↓) channel, and left (right) panels do not include (include) compressive strain. When $\eta = 0\%$, as shown in the left panels of Fig. 8, Te and Te′ have similar features. In the ↑ channel, near E_F the $m = \pm 1$ bands predominate in both occupied and unoccupied states. In the ↓ channel, bands near E_F are the unoccupied $m = 0$ state. Hence, $E_{\rm MCA} > 0$ results from $\langle m = \pm 1, \uparrow |L_z|m = \pm 1, \uparrow\rangle$ in the ↑ channel. In addition, a relatively small $E_{\rm MCA} > 0$ arises from $\langle m = \pm 1, \uparrow |L_x|m = 0, \downarrow\rangle$ via the spin-flip channel. As shown in Figs. 6(c) and 6(e), $\langle m = \pm 1|L_z|m = \pm 1\rangle$ gives $E_{\rm MCA} > 0$ within the same spin channel, and $\langle m = \pm 1|L_x|m = 0\rangle$ gives a small $E_{\rm MCA} > 0$ with the spin-flip channel.

When $\eta = -5\%$, as shown in right panels of Fig. 8, Te and Te′ exhibit a similar occupation change in the ↑ channel. As almost all $m = \pm 1$ bands become unoccupied, contributions from $\langle m = \pm 1, \uparrow | L_z | m = \pm 1, \uparrow \rangle$ disappear. Moreover, because the occupied $m = 0$ state gets near E_F, $\langle m = 0, \uparrow | L_x | m = \pm 1, \uparrow \rangle$ gives $E_{\mathrm{MCA}} < 0$. As shown in Figs. 6(d) and 6(f), $E_{\mathrm{MCA}} > 0$ contributions from $\langle m = \pm 1 | L_z | m = \pm 1 \rangle$ decrease. The contributions from $\langle m = 0 | L_x | m = \pm 1 \rangle$ also decrease when $\eta = -5\%$. The Te contribution remains positive, but that of Te′ becomes negative. To better understand the different signs of E_{MCA} from Te and Te′, the ↓ channel bands are discussed below.

In the ↓ channel, Te and Te′ exhibit slightly different occupation changes. For Te, bands in the ↓ channel shift downward, where some $m = 0$ bands become occupied. As such, $\langle m = 0, \downarrow | L_x | m = \pm 1, \uparrow \rangle$ results in $E_{\mathrm{MCA}} > 0$. Accordingly, $E_{\mathrm{MCA}} > 0$ is retained via spin-flip channels. However, in the case of Te′, bands in the ↓ channel shift upward. Unoccupied $m = 0$ bands move farther away from E_F, while occupied $m = \pm 1$ bands get closer to E_F. Consequently, $E_{\mathrm{MCA}} < 0$ arises from $\langle m = \pm 1, \downarrow | L_x | m = 0, \downarrow \rangle$. For Te′, $\langle m = 0 | L_x | m = \pm 1 \rangle$ gives $E_{\mathrm{MCA}} < 0$ in the same spin channels. Due to the contrasting behavior in the ↓ channel, Te in the monolayer retains $E_{\mathrm{MCA}} > 0$, while Te′ in the bilayer exhibits $E_{\mathrm{MCA}} < 0$ at $\eta = -5\%$.

V. CONCLUSIONS

The strain tunability of magnetocrystalline anisotropy of monolayer and bilayer Fe_3GeTe_2 was demonstrated in the framework of density functional theory calculations. Total magnetic moments decrease and increase under compressive and tensile strain, respectively. Among two inequivalent Fe atoms, Fe(I) showed a drastic change in moments under strain due to the occupation change of the minority spin state, while Fe(II) was almost insensitive to change. Fe_3GeTe_2 exhibits distinctive MCA for compressive and tensile strains. Due to bands shift caused by strain, monolayer and bilayer Fe_3GeTe_2 have strain-dependent E_{MCA}. For tensile strain, $E_{\mathrm{MCA}} > 0$ with little change in magnitude, whereas for compressive strain, E_{MCA} drops dramatically by 3.22 meV/f.u. (4.93 meV/f.u.) for the monolayer (bilayer). In particular, bilayer Fe_3GeTe_2 accompanies the sign change of E_{MCA}. MCA analysis was performed from three perspectives: atomic decomposition, SOC matrix analysis, and band analysis of occupation changes. With atomic decomposition, Te dominantly contributes to E_{MCA}. $E_{\mathrm{MCA}} > 0$ of Te is predominated by $\langle m = \pm 1, \uparrow | L_z | m = \pm 1, \uparrow \rangle$. For $\eta = -5\%$, the $\langle m = \pm 1, \uparrow | L_z | m = \pm 1, \uparrow \rangle$ contribution substantially decreases. Moreover, in the bilayer for $\eta = -5\%$, $E_{\mathrm{MCA}} < 0$ comes from $\langle m = \pm 1, \downarrow | L_x | m = 0, \downarrow \rangle$.

ACKNOWLEDGMENTS

We appreciate valuable discussions with S. C. Hong. This research was supported by the National Research Foundation (NRF) of Korea (Grants No. NRF-2019R1I1A3A01059880 and No. NRF-2022M3H4A1A04096339).

[1] B. Huang, G. Clark, E. Navarro-Moratalla, D. R. Klein, R. Cheng, K. L. Seyler, D. Zhong, E. Schmidgall, M. A. McGuire, D. H. Cobden *et al.*, Nature (London) **546**, 270 (2017).
[2] N. D. Mermin and H. Wagner, Phys. Rev. Lett. **17**, 1133 (1966).
[3] P. A. Joy and S. Vasudevan, Phys. Rev. B **46**, 5425 (1992).
[4] J.-U. Lee, S. Lee, J. H. Ryoo, S. Kang, T. Y. Kim, P. Kim, C.-H. Park, J.-G. Park, and H. Cheong, Nano Lett. **16**, 7433 (2016).
[5] K. Kim, S. Y. Lim, J.-U. Lee, S. Lee, T. Y. Kim, K. Park, G. S. Jeon, C.-H. Park, J.-G. Park, and H. Cheong, Nat. Commun. **10**, 345 (2019).
[6] B. L. Chittari, Y. Park, D. Lee, M. Han, A. H. MacDonald, E. Hwang, and J. Jung, Phys. Rev. B **94**, 184428 (2016).
[7] C. Gong, L. Li, Z. Li, H. Ji, A. Stern, Y. Xia, T. Cao, W. Bao, C. Wang, Y. Wang *et al.*, Nature (London) **546**, 265 (2017).
[8] J. M. Kosterlitz and D. J. Thouless, J. Phys. C **6**, 1181 (1973).
[9] M. Gibertini, M. Koperski, A. F. Morpurgo, and K. S. Novoselov, Nat. Nanotechnol. **14**, 408 (2019).
[10] K. S. Burch, D. Mandrus, and J.-G. Park, Nature (London) **563**, 47 (2018).
[11] P. Ajayan, P. Kim, and K. Banerjee, Phys. Today **69**(9), 38 (2016).
[12] Z. Fei, B. Huang, P. Malinowski, W. Wang, T. Song, J. Sanchez, W. Yao, D. Xiao, X. Zhu, A. F. May *et al.*, Nat. Mater. **17**, 778 (2018).
[13] H.-J. Deiseroth, K. Aleksandrov, C. Reiner, L. Kienle, and R. K. Kremer, Eur. J. Inorg. Chem. **2006**, 1561.
[14] A. F. May, S. Calder, C. Cantoni, H. Cao, and M. A. McGuire, Phys. Rev. B **93**, 014411 (2016).
[15] Y. Deng, Y. Yu, Y. Song, J. Zhang, N. Z. Wang, Z. Sun, Y. Yi, Y. Z. Wu, S. Wu, J. Zhu *et al.*, Nature (London) **563**, 94 (2018).
[16] X. Lin and J. Ni, Phys. Rev. B **100**, 085403 (2019).
[17] H. K. Gweon, S. Y. Lee, H. Y. Kwon, J. Jeong, H. J. Chang, K.-W. Kim, Z. Q. Qiu, H. Ryu, C. Jang, and J. W. Choi, Nano Lett. **21**, 1672 (2021).
[18] K. Kim, J. Seo, E. Lee, K.-T. Ko, B. S. Kim, B. G. Jang, J. M. Ok, J. Lee, Y. J. Jo, W. Kang *et al.*, Nat. Mater. **17**, 794 (2018).
[19] S. Laref, K.-W. Kim, and A. Manchon, Phys. Rev. B **102**, 060402(R) (2020).
[20] S. Y. Park, D. S. Kim, Y. Liu, J. Hwang, Y. Kim, W. Kim, J.-Y. Kim, C. Petrovic, C. Hwang, S.-K. Mo *et al.*, Nano Lett. **20**, 95 (2020).
[21] H. L. Zhuang, P. R. C. Kent, and R. G. Hennig, Phys. Rev. B **93**, 134407 (2016).
[22] Y.-P. Wang, X.-Y. Chen, and M.-Q. Long, Appl. Phys. Lett. **116**, 092404 (2020).
[23] G. Kresse and J. Furthmüller, Phys. Rev. B **54**, 11169 (1996).
[24] A. D. Becke, J. Chem. Phys. **85**, 7184 (1986).
[25] J. Klimeš, D. R. Bowler, and A. Michaelides, Phys. Rev. B **83**, 195131 (2011).
[26] D. Odkhuu, Sci. Rep. **8**, 6900 (2018).

[27] H. Yang, A. D. Vu, A. Hallal, N. Rougemaille, J. Coraux, G. Chen, A. K. Schmid, and M. Chshiev, Nano Lett. **16**, 145 (2016).

[28] B. Chen, J. Yang, H. Wang, M. Imai, H. Ohta, C. Michioka, K. Yoshimura, and M. Fang, J. Phys. Soc. Jpn. **82**, 124711 (2013).

[29] J. Yi, H. Zhuang, Q. Zou, Z. Wu, G. Cao, S. Tang, S. Calder, P. Kent, D. Mandrus, and Z. Gai, 2D Mater. **4**, 011005 (2016).

[30] See Supplemental Material at http://link.aps.org/supplemental/10.1103/PhysRevB.109.174434 for the following: Magnetic moments of Fe(II) are compared with those in an isolated Fe-Ge monolayer with PDOS. Fe(II) in an isolated Fe-Ge monolayer without neighboring atoms in the vertical directions exhibits a larger magnetic moment, $2.15\mu_B$. E_{MCA} with angle changes in the xz, yz, and xy planes is discussed. In both monolayer and bilayer Fe_3GeTe_2, E_{MCA} significantly changes by the spin rotation angles within the xz and yz planes. Magnetic moments under strain are presented with respect to the bond length of Fe(I)-Te and Fe(II)-Te. Magnetic moments of Fe(I) tend to increase with the distance of Fe(I)-Te.

[31] L. D. Landau and E. M. Lifshitz, *Electrodynamics for Continuous Media* (Pergamon, New York, 1975).

[32] D. S. Wang, R. Wu, and A. J. Freeman, Phys. Rev. B **47**, 14932 (1993).

[33] J. J. Sakurai and J. Napolitano, *Modern Quantum Mechanics*, 2nd ed. (Cambridge University Press, Cambridge, UK, 2017).

[34] V. Antropov, L. Ke, and D. Åberg, Solid State Commun. **194**, 35 (2014).